

## Supplemental Material

Zhentao Wang<sup>1</sup> and Cristian D. Batista<sup>1,2</sup>

<sup>1</sup>*Department of Physics and Astronomy, The University of Tennessee, Knoxville, Tennessee 37996, USA*

<sup>2</sup>*Quantum Condensed Matter Division and Shull-Wollan Center,  
Oak Ridge National Laboratory, Oak Ridge, Tennessee 37831, USA*

### I. CHARACTER TABLE OF $C_{4v}$ GROUP

The point group of Shastry-Sutherland lattice is  $C_{4v}$ , with 5 classes of symmetry operations: identity  $E$ , two rotations  $\{C_4, C_2\}$  and two reflections  $\{\sigma_v, \sigma_d\}$  (see Table. I).

	$E$	$C_2$	$2C_4$	$2\sigma_v$	$2\sigma_d$
$A_1 [1]$	1	1	1	1	1
$A_2 [xy(x^2 - y^2)]$	1	1	1	-1	-1
$B_1 [x^2 - y^2]$	1	1	-1	1	-1
$B_2 [xy]$	1	1	-1	-1	1
$E [x, y]$	2	-2	0	0	0

Table I. Character table of group  $C_{4v}$  [1].

### II. CHOICE OF INITIAL BASIS

The initial basis is always chosen such that it does not break the point group symmetries explicitly. The choices for different values of  $S_{\text{tot}}^z$  are listed in Figs. S1, S2 and S3.

### III. CONSTRUCTION OF ORDER PARAMETERS

In the  $J'/J \ll 1$  limit, the  $S_{\text{tot}} = 2$ ,  $\mathbf{k} = (\pi, \pi)$ , IREP  $E$  states are known from Ref. [2]. Besides the  $S_{\text{tot}}^z = 2$  initial states shown in Fig. S3, there is another set of relevant states (see Fig. S4) generated at  $M = 2$ . Here we write down the diagonalized wavefunctions for  $\mathbf{Q} \equiv (\pi, \pi)$ :

$$|\Psi_1(\mathbf{Q})\rangle_{S2E} \approx \alpha \left[ |\varphi_7^{(2)}(\mathbf{Q})\rangle + |\varphi_8^{(2)}(\mathbf{Q})\rangle \right] + \beta \left[ |\varphi_2^{(2)}(\mathbf{Q})\rangle - |\varphi_1^{(2)}(\mathbf{Q})\rangle \right], \quad (\text{S1a})$$

$$|\Psi_2(\mathbf{Q})\rangle_{S2E} \approx \alpha \left[ |\varphi_6^{(2)}(\mathbf{Q})\rangle - |\varphi_5^{(2)}(\mathbf{Q})\rangle \right] + \beta \left[ |\varphi_4^{(2)}(\mathbf{Q})\rangle - |\varphi_3^{(2)}(\mathbf{Q})\rangle \right], \quad (\text{S1b})$$

where

$$|\varphi_i^{(S_z)}(\mathbf{Q})\rangle = \frac{\hat{P}_{\mathbf{Q}} |\varphi_i^{(S_z)}\rangle}{\sqrt{\langle \varphi_i^{(S_z)} | \hat{P}_{\mathbf{Q}} | \varphi_i^{(S_z)} \rangle}}. \quad (\text{S2})$$

The above wavefunctions have  $S_{\text{tot}} = 2$ , as long as the normalization condition  $2|\alpha|^2 + 2|\beta|^2 = 1$  is satisfied. The values

of  $\alpha, \beta$  depend on  $J'/J$  [2]. To construct the nematic order parameter, we only need a bound state wavefunction that has significant overlap with the exact one. We then choose  $\alpha = 0.7$ ,  $\beta = 0.1$  to construct the order parameter

$$A_{\mathbf{Q}}^{S2E} \equiv |\Psi_1(\mathbf{Q})\rangle_{S2E} \langle 0|, \quad (\text{S3})$$

The momentum dependence of the corresponding susceptibility is obtained by computing the two-point correlator after replacing  $\mathbf{Q}$  with  $\mathbf{k}$ .

We have demonstrated in the main text that the lowest bound state wave function has  $S_{\text{tot}} = 2$ ,  $\mathbf{k} = (0, 0)$ , IREP  $A_2$  for larger values of  $J'/J$ . Similarly, with the eight states in Figs. (S3)(S4), we can write down the approximate  $\mathbf{K} \equiv (0, 0)$  wavefunction :

$$|\Psi(\mathbf{K})\rangle_{S2A_2} = \alpha \left[ |\varphi_5^{(2)}(\mathbf{K})\rangle - |\varphi_6^{(2)}(\mathbf{K})\rangle - |\varphi_7^{(2)}(\mathbf{K})\rangle + |\varphi_8^{(2)}(\mathbf{K})\rangle \right] + \beta \left[ -|\varphi_1^{(2)}(\mathbf{K})\rangle - |\varphi_2^{(2)}(\mathbf{K})\rangle + |\varphi_3^{(2)}(\mathbf{K})\rangle + |\varphi_4^{(2)}(\mathbf{K})\rangle \right]. \quad (\text{S4})$$

Once again,  $S_{\text{tot}} = 2$  is guaranteed by the normalization con-

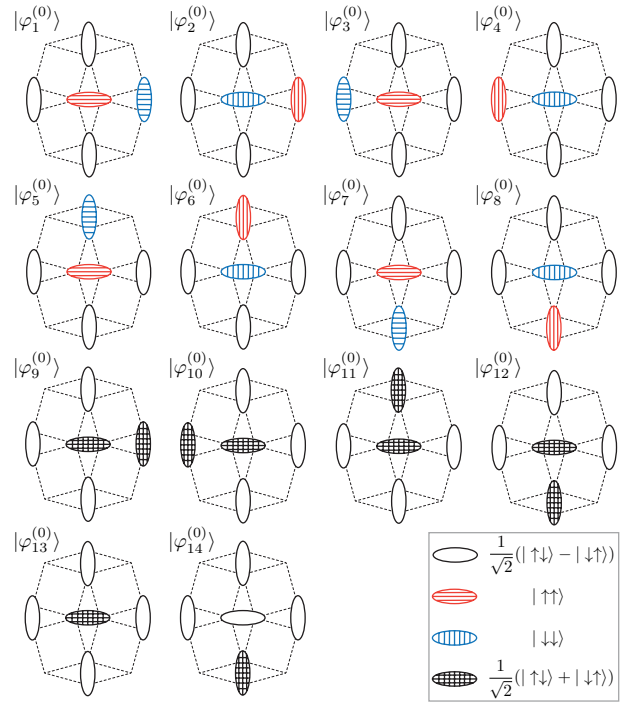


Figure S1. The  $S_{\text{tot}}^z = 0$  initial basis chosen in this Letter.

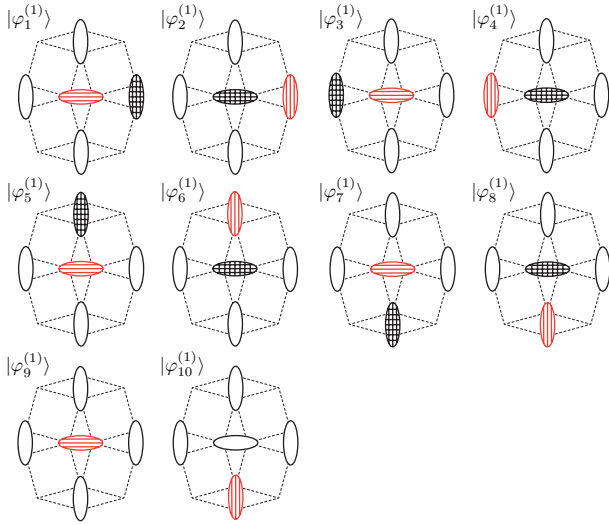


Figure S2. The  $S_{\text{tot}}^z = 1$  initial basis chosen in this Letter. The notations are following Fig. S1.

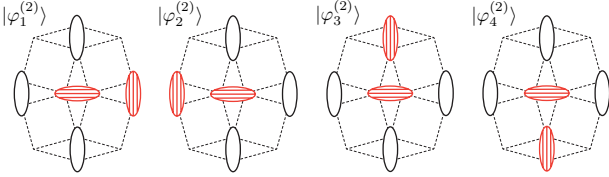


Figure S3. The  $S_{\text{tot}}^z = 2$  initial basis chosen in this Letter. The notations are following Fig. S1.

dition  $4|\alpha|^2 + 4|\beta|^2 = 1$ . To construct the corresponding order parameter  $A_k^{S2A_2}$ , we use  $\alpha = 0.47$ ,  $\beta = 0.17$  in the main text.

We note that the exact bound state in this region (larger  $J'/J$ ), has a larger size than the one in the  $J'/J \ll 1$  limit. Consequently,  $A_k^{S2A_2}$  produces more spectral weight at high energies in comparison to  $A_k^{S2E}$  (see Fig. 5c).

For even larger  $J'/J$  with  $h = 0$ , the lowest states have  $S_{\text{tot}} = 0$ ,  $\mathbf{k} = (0, 0)$ , IREP  $A_2$ . we can similarly construct the approximate wavefunction at  $\mathbf{K} \equiv (0, 0)$ :

$$\begin{aligned}
 |\Psi(\mathbf{K})\rangle_{S0A_2} &= \alpha \left[ |\varphi_1^{(0)}(\mathbf{K})\rangle + |\varphi_2^{(0)}(\mathbf{K})\rangle + |\varphi_3^{(0)}(\mathbf{K})\rangle + |\varphi_4^{(0)}(\mathbf{K})\rangle \right. \\
 &\quad \left. - |\varphi_5^{(0)}(\mathbf{K})\rangle - |\varphi_6^{(0)}(\mathbf{K})\rangle - |\varphi_7^{(0)}(\mathbf{K})\rangle - |\varphi_8^{(0)}(\mathbf{K})\rangle \right] \\
 &\quad - \beta \left[ |\varphi_9^{(0)}(\mathbf{K})\rangle + |\varphi_{10}^{(0)}(\mathbf{K})\rangle - |\varphi_{11}^{(0)}(\mathbf{K})\rangle - |\varphi_{12}^{(0)}(\mathbf{K})\rangle \right]. \quad (\text{S5})
 \end{aligned}$$

In this case, the normalization condition  $8|\alpha|^2 + 4|\beta|^2 = 1$  is different from the  $S_{\text{tot}} = 0$  condition, which requires  $\alpha = \beta$ . Combining both conditions we have  $\alpha = \beta = \frac{1}{2\sqrt{3}}$ .

Once again, since this approximate wavefunction has a reduced overlap with the exact bound state, we see a significant amount of spectral weight at high energies in Fig. 5a in the main text.

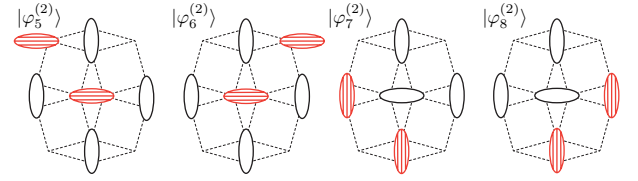


Figure S4. The extra  $S_{\text{tot}}^z = 2$  states for the approximate  $S_{\text{tot}} = 2$  bound state. The notations are following Fig. S1.

#### IV. DOMINANT INSTABILITY AT ZERO FIELD

In the  $S_{\text{tot}} = 0$  sector at  $h = 0$ , we can roughly estimate  $J'_c/J \approx 0.69$  in the  $M \rightarrow \infty$  limit (see Fig. 3 in the main text). At this point  $J'/J = 0.69$ , we show in Fig. S5 that the gaps of the other  $S_{\text{tot}}$  sectors remain finite in the  $M \rightarrow \infty$  limit, even with a linear extrapolation. Note that the calculation converges for large enough  $M$ , implying that the slopes of the curves in Fig. S5 should finally become zero. In other words, the true value of the gaps should be larger than that obtained from linear extrapolation. Since all other gaps remain finite while the  $S_{\text{tot}} = 0$  gap is closing, we can safely conclude that the order parameter with highest susceptibility has  $S_{\text{tot}} = 0$  for  $h = 0$ .

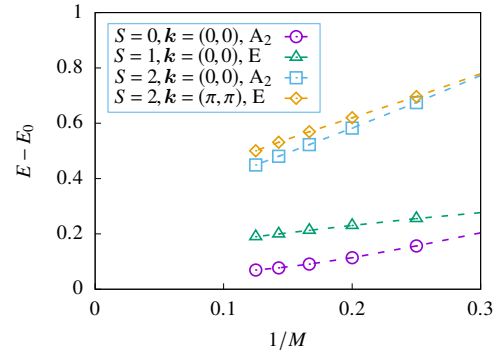


Figure S5. Gaps of the four candidate states at  $J'/J = 0.69$ ,  $h = 0$ .

#### V. CONVERGENCE OF DYNAMIC STRUCTURE FACTORS

Generally, the convergence speed of the DSFs is determined by  $\xi$ . Larger  $\xi$  values require larger number of iterations ( $M$ ) to obtain qualitatively correct results. For instance,  $\chi_{S2E}(\mathbf{k}, \omega)$  is almost fully converged at  $M = 3$  and  $J'/J = 0.2$  (see Fig. 5d in the main text) because  $\xi$  is a few lattice spaces.

To have a more quantitative sense of the convergence as a function of  $M$ , we first benchmark the DSF  $S^{++}(\mathbf{k}, \omega)$  with  $J'/J = 0.63$ ,  $h = 0$ , which is relevant for the compound  $\text{SrCu}_2(\text{BO}_3)_2$  [3]. In Fig. S6, we show the evolution of the calculated  $S^{++}(\mathbf{k}, \omega)$  as a function of  $M$ . The lowest single and two-triplon bands are already converged at  $M = 5$ . We note that the method produces not only the bound states, but also

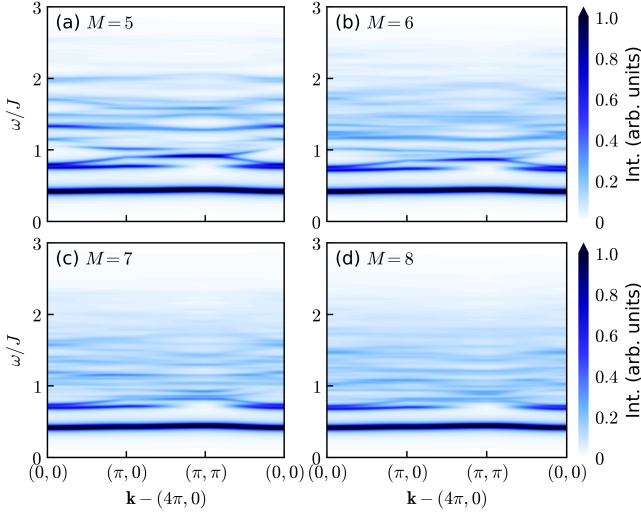


Figure S6.  $T = 0$  DSF  $S^{--}(\mathbf{k}, \omega)$  for  $J'/J = 0.63$ ,  $h = 0$ , at four different iterations  $M = \{5, 6, 7, 8\}$ . Lorentzian broadening factor  $\eta = 0.02J$  is used.

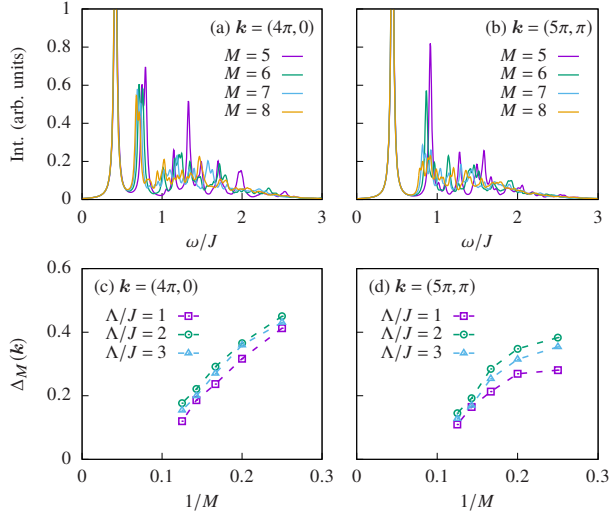


Figure S7. (a)(b) Linecuts of Fig. S6 at two momenta. (c)(d) The relative error  $\Delta_M(\mathbf{k})$  calculated at the two momenta, with three different choices of cutoff  $\Lambda$ .

the multi-triplon continuum, which is qualitatively captured at  $M = 5$  and about to converge at  $M \gtrsim 8$  for the parameters used in Fig. S6.

To measure the relative change between different iterations, we can define

$$\Delta_M(\mathbf{k}) = \sqrt{\frac{1}{\Lambda} \int_0^\Lambda d\omega \left( \frac{S^{--}(\mathbf{k}, \omega)_M - S^{--}(\mathbf{k}, \omega)_{M-1}}{S^{--}(\mathbf{k}, \omega)_M + S^{--}(\mathbf{k}, \omega)_{M-1}} \right)^2}, \quad (\text{S6})$$

where  $\Lambda$  is the energy cutoff. For the fully converged result, it is expected that  $\Delta_M(\mathbf{k}) \rightarrow 0$ .

In Fig. S7, we show the linecuts of Fig. S6 at two momenta:  $\mathbf{k} - (4\pi, 0) = (0, 0)$  and  $(\pi, \pi)$ . Correspondingly, the relative errors  $\Delta_M(\mathbf{k})$  are shown in the bottom panels of the same

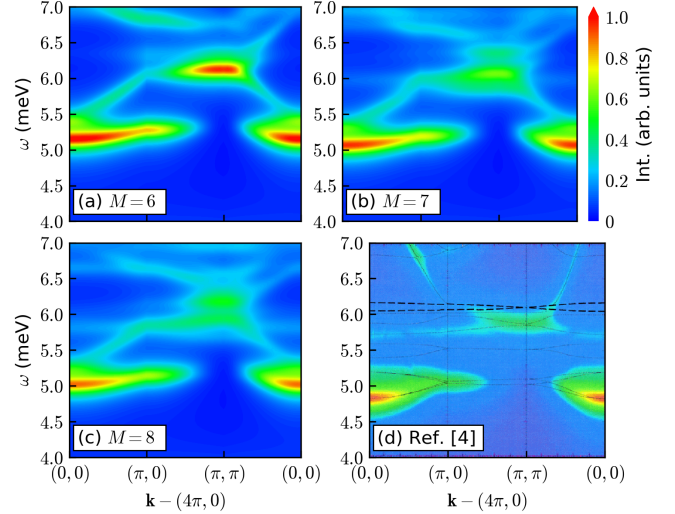


Figure S8. (a-c)  $T = 0$  DSF  $S^{zz}(\mathbf{k}, \omega)$  calculated using same parameters as Ref. [4]:  $J = 6.16\text{meV}$ ,  $J'/J = 0.603$ ,  $h = 0$ . Lorentzian broadening factor  $\eta = 0.02J$  is used. (d)  $S^{zz}(\mathbf{k}, \omega)$  reproduced from Ref. [4].

figure. The relative errors decrease rapidly as we increase  $M$ , reaching around 15% at  $M = 8$ . We note that the value of  $\Delta_M(\mathbf{k})$  depends on the energy cutoff  $\Lambda$ : the lowest relative errors in Fig. S7 are found when  $\Lambda/J = 1$ , consistent with the fact that low-energy excitations converge faster than the high-energy ones. Note also that  $\Delta_M(\mathbf{k})$  depends heavily on the choice of Lorentzian broadening factor used in the DSF calculation: larger broadening factors lead to smaller relative errors.

It is also worth benchmarking with Ref. [4], which carried out the DSF calculation for SSM using the perturbative CUTs. Figure S8 shows a good qualitative agreement. However, there are two small differences: the band near 5meV produced by our method is slightly higher than that obtained from CUT, which could arise from incomplete convergence for  $M \lesssim 8$  in our method or missing higher order corrections in CUT. We also note that our method captures more accurately the states in the continuum.

## VI. COMPETING CHIRAL STATE

The main text describes the  $S_{\text{tot}} = 1$  instability that leads to the stripe magnetic order. As shown in Fig. 5(b), the lowest instability from the DSF arises from condensation of the  $\mathbf{k} = (0, 0)$  mode. Figure S9 examines this point in more detail. Besides reproducing Fig. 5(b) in higher resolution, we also denote the symmetries of the  $\mathbf{k} = (4\pi, 0)$  peaks [ $\mathbf{k} = (0, 0) \equiv (4\pi, 0)$ ].

As we mentioned in the main text, the state that produces the lowest peak at  $\mathbf{k} = (4\pi, 0)$  belongs to the IREP  $E$ . In Fig. S9, we see that the next peak at  $\mathbf{k} = (4\pi, 0)$  corresponds to the IREP  $B_1$  [with negligible weight at  $\mathbf{k} = (4\pi, 0)$ ]. Up to  $M = 8$ ,

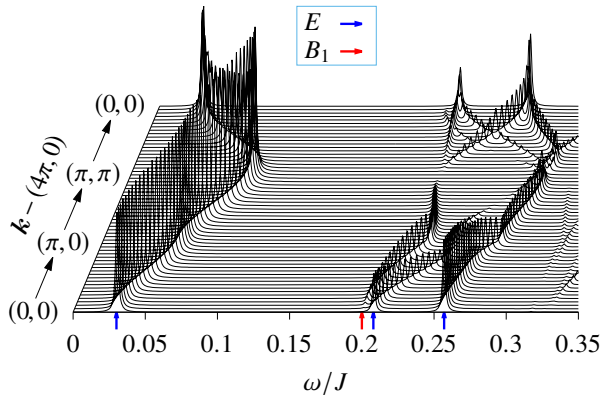


Figure S9.  $T=0$  DSF  $S^{+-}(\mathbf{k}, \omega)$  calculated at  $M = 8$ . The parameters are the same as in Fig. 5(b) in the main text:  $J'/J = 0.67$ ,  $h/J = 0.25$ . For better resolution, the Lorentzian broadening factor is chosen as  $\eta = 0.001J$  in this plot. The IREPs of the  $\mathbf{k} = (4\pi, 0)$  peaks are labeled by the arrows.

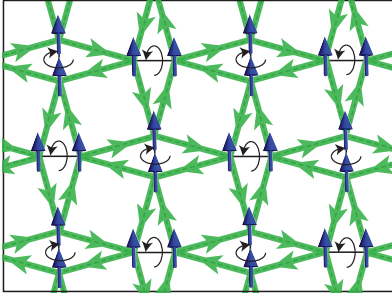


Figure S10. Schematic plot of the chiral phase. The bonds with arrow denote the sign of the vector chirality  $\langle (\mathbf{S}_i \times \mathbf{S}_j) \cdot \hat{z} \rangle$ .

we find that this  $B_1$  peak is always higher in energy (lower susceptibility) than the one corresponding to the IREP  $E$ . It is worth mentioning that condensation of the  $B_1$  state leads to the vector chiral ordering depicted in Fig. S10.

- 
- [1] J. P. Elliott and P. G. Dawber, *Symmetry in Physics*, Vol. 1 (Macmillan Press LTD, 1979).
  - [2] T. Momoi and K. Totsuka, *Phys. Rev. B* **62**, 15067 (2000).
  - [3] P. Corboz and F. Mila, *Phys. Rev. Lett.* **112**, 147203 (2014).
  - [4] C. Knetter and G. S. Uhrig, *Phys. Rev. Lett.* **92**, 027204 (2004).